

See discussions, stats, and author profiles for this publication at: <https://www.researchgate.net/publication/274571025>

Ultrafast Imaging of Surface Plasmons Propagating on a Gold Surface

ARTICLE *in* NANO LETTERS · APRIL 2015

Impact Factor: 13.59 · DOI: 10.1021/acs.nanolett.5b00803 · Source: PubMed

READS

104

5 AUTHORS, INCLUDING:



Yu Gong

City University of New York - Hunter College

26 PUBLICATIONS 118 CITATIONS

[SEE PROFILE](#)



Dehong Hu

Pacific Northwest National Laboratory

89 PUBLICATIONS 4,676 CITATIONS

[SEE PROFILE](#)



Wayne Hess

Pacific Northwest National Laboratory

144 PUBLICATIONS 1,694 CITATIONS

[SEE PROFILE](#)

Ultrafast Imaging of Surface Plasmons Propagating on a Gold Surface

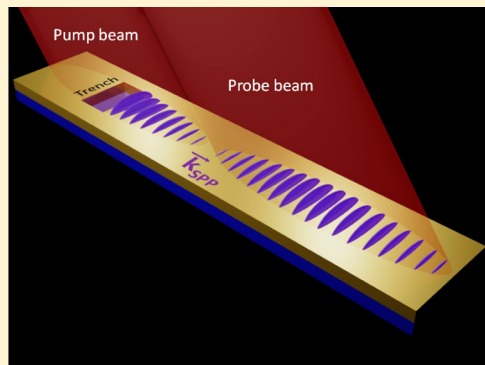
Yu Gong,[†] Alan G. Joly,[†] Dehong Hu,[‡] Patrick Z. El-Khoury,[†] and Wayne P. Hess^{*,†}

[†]Physical Sciences Division, [‡]Environmental Molecular Sciences Laboratory, Pacific Northwest National Laboratory, P.O. Box 999, Richland, Washington 99352, United States

 Supporting Information

ABSTRACT: We record time-resolved nonlinear photoemission electron microscopy (tr-PEEM) images of propagating surface plasmons (PSPs) launched from a lithographically patterned rectangular trench on a flat gold surface. Our tr-PEEM scheme involves a pair of identical, spatially separated, and interferometrically locked femtosecond laser pulses. Power-dependent PEEM images provide experimental evidence for a sequential coherent nonlinear photoemission process, in which one laser source launches a PSP through a linear interaction, and the second subsequently probes the PSP via two-photon photoemission. The recorded time-resolved movies of a PSP allow us to directly measure various properties of the surface-bound wave packet, including its carrier wavelength (783 nm) and group velocity (0.95c). In addition, tr-PEEM images reveal that the launched PSP may be detected at least 250 μ m away from the coupling trench structure.

KEYWORDS: Propagating surface plasmon, time-resolved, sub-femtosecond, PEEM



Surface plasmons propagate at speeds nearing the speed of light¹ and can be confined to subwavelength dimensions using engineered metal nanostructures.² Whereas the first property is attractive for signal processing applications^{3–5} and for the construction of plasmonic nanocircuits,^{5,6} the second enables ultrasensitive chemical and biological detection and imaging.^{7–10} By virtue of their nanoscopic and dissipative nature, a detailed characterization of surface plasmons requires the development of ultrafast nanoscopic tools, i.e., high-resolution microscopic techniques capable of recording images at time scales on the order of a few optical cycles. In this regard, several techniques have been developed and/or adapted to probing the various spatiotemporal characteristics of surface plasmons. These include dark field scattering microscopy,¹¹ fluorescence microscopy,^{12–14} coherent anti-Stokes Raman scattering microspectroscopy,^{15,16} near-field scanning optical microscopy,¹⁷ and photoemission electron microscopy (PEEM).^{18–20}

Among these techniques, PEEM has the advantage of resolving surface plasmons with high spatial resolution, and without the need for molecular reporters or scanning probes,^{21–23} both of which may potentially bias surface plasmon properties derived from such measurements. PEEM directly maps surface plasmons through nonlinear photoemission, with typical spatial resolutions on the order of tens of nanometers. As photoemission is induced by a nonlinear process, it is also possible to directly image surface plasmon propagation dynamics using a variant of this technique, namely, through time-resolved nonlinear photoemission electron microscopy (tr-PEEM).²³ In effect, tr-PEEM can be used to

record movies of propagating surface plasmons (PSPs) in real time and on nanometer scales. Herein, we report such measurements.

PSPs can be launched from specific locations at the metal–vacuum interface, where engineered nanoscale coupling structures such as slits, trenches, or holes are sited.^{24–26} Once launched,^{18,27–30} PSPs have been shown to propagate pseudounidirectionally on smooth metal surfaces with low longitudinal and transverse dispersion.^{13,17} Provided PSPs have sufficient propagation length, they may be transported and subsequently coupled to optical elements. This property has been exploited, for example, in applications requiring excitation sources that are remote from the initial coupling site.³¹ The propagation length is primarily determined by the imaginary (absorptive) component of the metal dielectric function at the PSP oscillation frequency.³² Although the generation, propagation, focusing, and possible control of PSPs has been described in some detail,^{18,19,29,33–37} direct experimental measurements of fundamental PSP properties such as their energies, bandwidths, and propagation lengths are limited.

In this work, we record movies of PSPs propagating on gold surfaces using tr-PEEM. PSPs are coupled into gold films using a large ($10 \times 8 \mu\text{m}^2$) lithographically patterned rectangular trench. Three photons ($h\nu = 1.55 \text{ eV}$) are required to induce photoemission. The first photon (termed the “pump” pulse from hereon) is provided by an ultrafast laser pulse centered at

Received: February 27, 2015

Revised: March 31, 2015

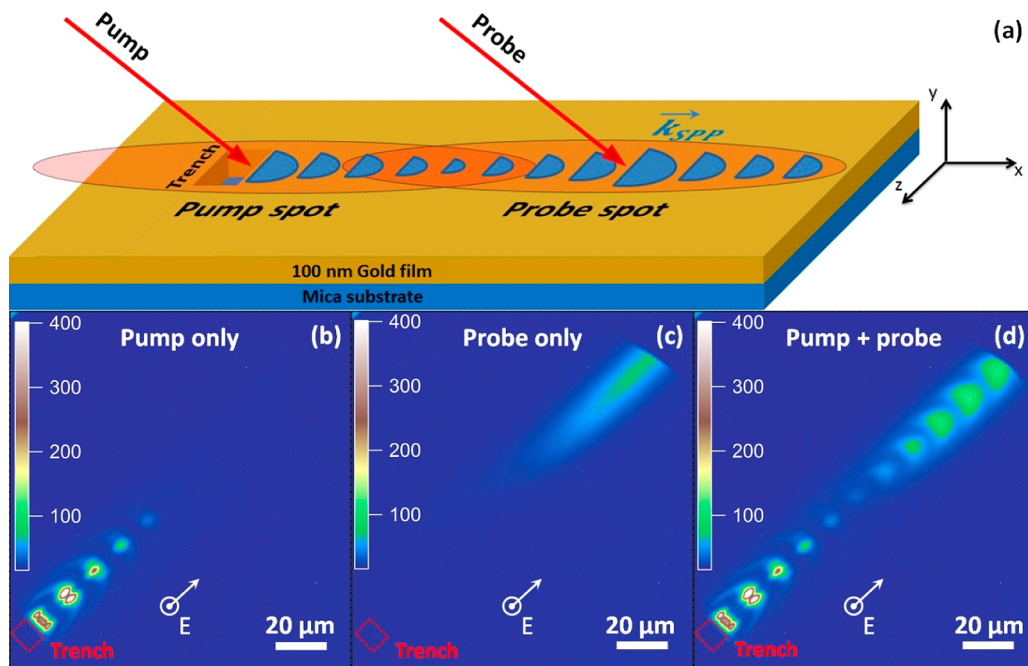


Figure 1. (a) Schematic of our experiments: the pump pulse and probe pulse are spatially separated. The PSP generated by the pump pulse is detected by the probe at more than one hundred microns away from the plasmonic trench structure. PEEM images of (b) photoemission interference patterns from a $10 \times 8 \text{ }\mu\text{m}^2$ trench due to the PSP wave packet excited by the pump beam. (c) Photoemission from a flat gold surface generated by the probe beam about $150\text{ }\mu\text{m}$ away from the trench (no pump beam). (d) Photoemission interference pattern when pump and probe are applied together. The pattern at the probe beam position indicates the interference of the probe beam and PSP wave packet launched at the trench following excitation by the pump beam. The red dash squares represent the trench position. Pump and probe pulses are polarized with electric vector parallel to the out-of-plane axis (p-polarization). Laser pulses propagate from the lower left to the upper right in b–c.

the trench. A second spatially separated interferometrically locked laser source (termed the “probe” pulse from hereon) provides the two additional photons required to achieve nonlinear photoemission from the metal surface. This picture is experimentally demonstrated through power-dependent PEEM images, which reveal that the PSP is launched via a linear interaction process with the pump pulse centered at the coupling structure. Overall, time-integrated and time-resolved PEEM images combined with finite-difference time domain simulations together allow us to directly extract various fundamental properties of PSPs.

Figure 1 shows a schematic representation of our experimental geometry and PEEM images recorded following irradiation with (i) pump pulse only, (ii) probe pulse only, and (iii) both pump and probe pulses. Ultrafast excitation of the trench structure with pump pulses launches surface plasmon wave packets that propagate in the x -direction. The probe is spatially and temporally offset from the pump, affording time-resolved imaging of launched PSPs at distances more than $100\text{ }\mu\text{m}$ away from the coupling trench structure. In this regard, our experimental and detection schemes are distinct from previously reported tr-PEEM experiments, in which the pump and probe pulses are spatially overlapped and are essentially indistinguishable. The advantage of the scheme employed herein includes (i) it extends the spatial detection limit beyond the laser spot size and (ii) it can be used to probe PSPs in regions that are remote from the coupling structure.

Figure 1b shows a PEEM image recorded following ultrafast laser irradiation ($\lambda = 800\text{ nm}$) of a rectangular trench milled into a 100 nm thick gold film with a single (pump) laser source. As noted in prior reports,^{18,19,28,29,34} the same laser pulse also illuminates a larger area of the flat metal surface, including

regions beyond the coupling structure. In this picture, the pump pulse not only launches the PSP but also interferes with the surface-bound wave packet beyond the coupling structure. It is this interference that governs our recorded images.²⁹ As illustrated in the ensuing discussion, the disappearance of the interference signal in Figure 1b is primarily a consequence of the finite laser spot size, third-order power dependence, and PSP propagation.

Figure 1c displays a PEEM image recorded following nonlinear probe-only excitation of the flat gold film in a region $100\text{--}200\text{ }\mu\text{m}$ beyond the rectangular trench coupling structure. Only the first half of the elliptical pump laser spot is visible within the largest PEEM field of view of $\sim 150\text{ }\mu\text{m}$. Figure 1d displays the PEEM image recorded following combined pump and probe excitation. In this case, the spatially offset probe pulse is temporally delayed by approximately 433 fs from the pump pulse, such that it arrives at the gold surface at the same time as the PSP generated by the pump pulse at the trench position. Photoemission from the polarization state prepared by the probe pulse and the PSP wave packet is clearly observable in the upper right region of Figure 1d. This demonstrates that the PSP wave packet propagates at least $150\text{ }\mu\text{m}$ from its original launching point. The 2D spatial profile of the imaged PSP is affected by (i) the elliptical profiles of the laser spots, incident onto the sample surface at a low angle of incidence, (ii) the profile of the launched PSP, (iii) convolution with pump and probe pulses, and (iv) interference with PSP waves launched from the upper and lower corners of the trench. The last effect is most evident in the second interference fringe closest to the trench, where a double-lobed pattern (and a nodal plane) is visible.

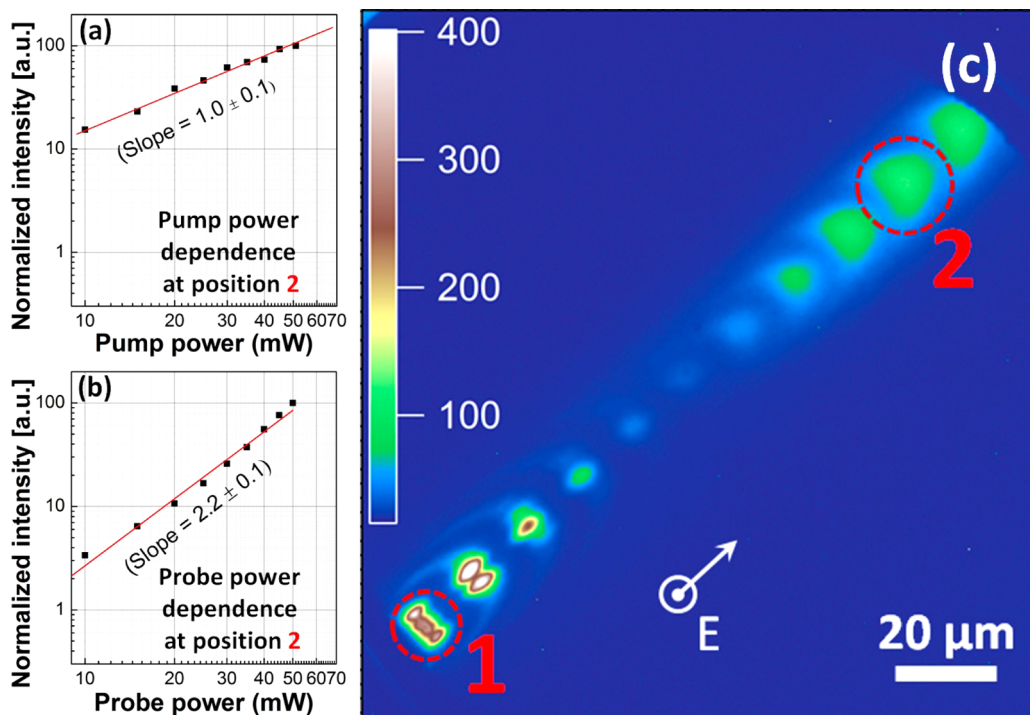


Figure 2. (a–b) Pump and probe power dependence on photoemission measured at position 2 as highlighted using dashed red circles in the (c) PEEM image of plasmonic trench under illumination of spatially separated pump and probe pulse. The reported error range corresponds to a single standard deviation.

The image in Figure 1d can be further analyzed to determine the carrier frequency of the PSP wave packet. The interference fringes between the light and PSP wave packet recur regularly at a spacing of $14.1 \mu\text{m}$, and their width monotonically increases with distance (see Supporting Information). The experimentally measured recurrence wavelength of $14.1 \mu\text{m}$ corresponds to the difference frequency between the laser (800 nm) and PSP fields. This is in good agreement with a value of $14.4 \mu\text{m}$ calculated using recently measured optical constants.³⁸ Using the experimentally determined value of $14.1 \mu\text{m}$, we calculate a PSP carrier wavelength of 783 nm . The increase in width is attributed to dispersive PSP propagation. The temporal width of the initial PSP wave packet is primarily determined by the excitation laser pulse, featuring a pulse width of 15 fs (fwhm). The wavepacket broadens during propagation, as reflected by increasingly broad interference fringes as a function of propagation distance; see Figure S2 of the Supporting Information section.

At least three 800 nm photons are required to induce photoemission from gold. For a single laser beam experiment (or two-beam excitation with indistinguishable beams), a coherent three photon photoemission process has been postulated to be the dominant mechanism.²⁸ For a three-photon process, the photoemission intensity, I_p , is proportional to the sixth power of the total polarization field integrated over time (following the discussion in ref 19).

$$I_p = \alpha \int_{-\infty}^{+\infty} [P_{\text{laser}} + P_{\text{PSP}}]^6 dt \quad (1)$$

Here P_{laser} is the polarization induced by the laser field, P_{PSP} is the polarization of the PSP including both coherent and incoherent contributions, and α is a proportionality constant that accounts for the overall detection efficiency.²⁸ In this report, the two beams are spatially separated. Therefore, power

dependent imaging using the distinct beams can be particularly informative about what process(es) contribute to the nonlinear time-resolved PEEM images. Figure 2 displays a PEEM image with two highlighted regions, marked 1 and 2. At position 1, the pump laser alone induces all observed photoemission and a three-photon power dependence, $I_p = \alpha \times P^n$ with $n = 3.2 \pm 0.1$ (≈ 3) is derived from the slope of the log–log plot of photoemission intensity versus pump laser power (see the Supporting Information). Although gold nominally has a work function of near 5 eV , this value is dependent on sample preparation and photoemission is readily observed for combined photon energies of less than 5 eV .³⁹ At position 2, we measure the photoemission yield dependence on pump laser power with the probe laser power fixed and the probe laser power dependence with the pump laser power fixed. The results are presented as log–log plots in Figure 2a and b, respectively.

The photoemission intensity at position 2 can be characterized by the relation: $I_p = c \cdot P_{\text{probe}}^n \times c' P_{\text{pump}}^{n'}$ where $n = 1.0 \pm 0.1$ (≈ 1), $n' = 2.2 \pm 0.1$ (≈ 2), and c and c' are proportionality constants that account for the efficiencies of (i) coupling the pump pulse, (ii) propagation of the generated surface plasmon, and (iii) probe–pulse induced two-photon photoemission of the propagated PSP wave packet. It is clear that the PSP launched by the pump laser results from a strictly linear interaction, while the probe pulse interacts quadratically with the launched PSP to induce photoemission. The distinct power laws for pump and probe lasers at position 2 suggest that a sequential coherent photoemission process is taking place; a coherent PSP wave packet is generated through a first-order interaction, propagates in space (and time), and is subsequently detected via multiphoton photoemission. It has been previously proposed that initial photoexcitation populates an intermediate polarization state, located between the Fermi and vacuum

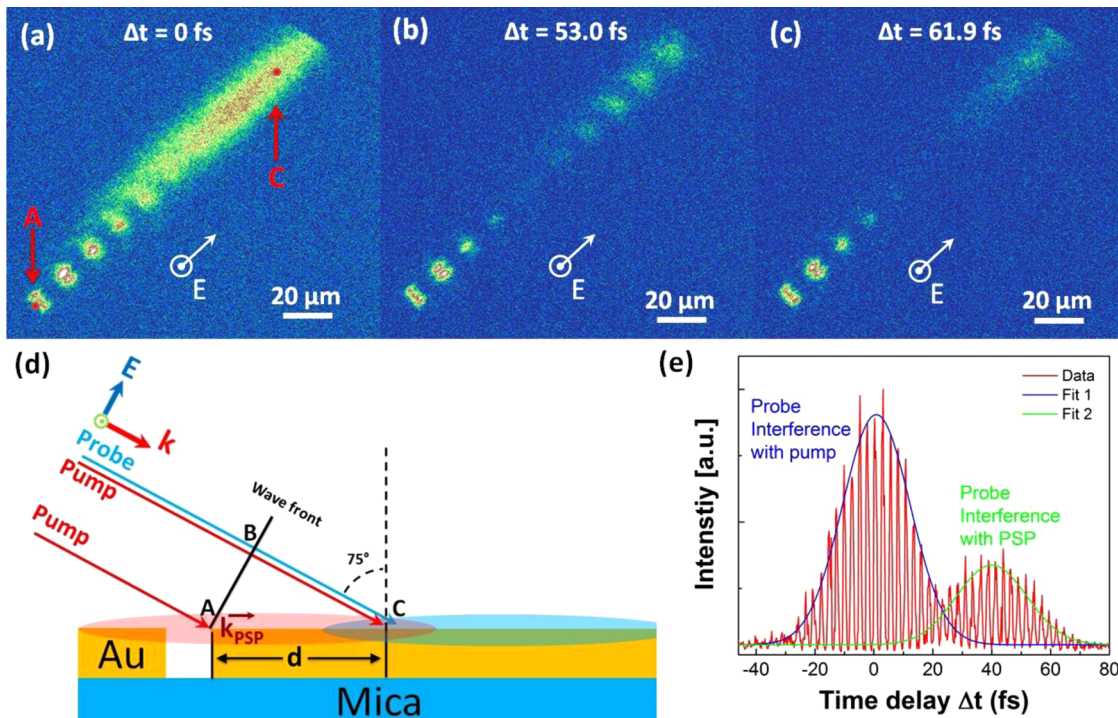


Figure 3. (a–c) TR-PEEM data of the plasmonic trench structure when applying pump and probe laser fields with a center-to-center separation of approximately 150 μm . Both pump and probe laser pulses propagate from left to right as indicated by the white arrow symbol. The $\Delta t = 0$ is defined as the time when probe and pump pulses are temporally overlapped at 135 μm away from the plasmonic trench coupling structure. (d) Schematic of double interference geometry: probe pulse with pump pulse and probe pulse with the PSP wave packet. The pump spot and probe spot are presented in red and blue color, respectively. (e) Interferometric photoemission intensity as a function of time at position 135 μm from the plasmonic trench. The two Gaussian fits of the field envelope indicate the time when the probe pulse interferes with pump (blue) and PSP wave packet (green).

levels, and subsequent photoexcitation induces photoemission from that state.⁴⁰ Our measurements and analysis are consistent with this picture.

Figure 3a–c displays tr-PEEM images recorded at different pump–probe delay times. These images can be rationalized on the basis of the schematic drawn in Figure 3d. We define $t = t_0$ as the time at which the pump pulse strikes the trench and $\Delta t = 0$ as the delay time at which the pump and probe pulses simultaneously arrive at point C, highlighted in Figure 3d. Due to the 75° angle of incidence, the pump beam features a large spatial distribution (spot size) in the propagation direction. Within the pump beam, as shown in Figure 3d, the wavefront of the pulse at positions A and B are synchronized. At t_0 , the pump at position A strikes the coupling structure and launches a PSP wave packet while the pump wavefront at position B travels until it reaches position C at the surface. The pump pulse at position B travels at the speed of light in vacuum, covering a distance $d \sin(75^\circ)$ until it arrives at position C on the surface, while the PSP wave packet at position A travels slower than the speed of light over a distance d , until it reaches position C. Although the pump and probe beams are spatially separated, there is a small amount of field overlap in the vicinity of position C. As such, the probe beam at position C interferes with the pump beam at a different time delay when compared to the PSP wave packet launched from position A.

Figure 3a displays the tr-PEEM image obtained when the pump and probe pulses simultaneously arrive at point C ($\Delta t = 0$, $d = 135 \mu\text{m}$). The PSP-light interference pattern is only detected in the region of the pump pulse spot, as the probe pulse arrives prior to surface plasmon propagation into the

probe pulse region. However, the overlap of the edges of the pump and probe pulses at point C and $\Delta t = 0$ is manifest as the large elliptical region of high photoemission observed in the upper right-hand corner of Figure 3a. Figure 3b displays the analogous image obtained when $\Delta t = 53.0 \text{ fs}$. In this case, the probe pulse interferes with the PSP wave packet launched from point A, as is evident in the upper right region of 3b. At a time delay of approximately 61.9 fs, only the tail of the PSP wave packet interferes with the probe, leading to a weak interference pattern in the upper right corner of Figure 3c. A time series of progressively delayed images forms a movie of surface plasmon propagation; see the Supporting Information section.

Figure 3e shows the time-resolved photoemission intensity as a function of delay time between the pump and probe pulses, measured at point C. The distance $d = 135 \mu\text{m}$ is measured using the PEEM image, calibrated to a reference SEM image, and is accurate to $\pm 1 \mu\text{m}$. The photoemission intensity displays a twin-peaked interferogram structure associated with the temporal overlap of pump and probe pulses in conjunction with the pump-pulse-launched PSP overlapped with the probe pulse. From the interferogram in Figure 3e, we know that the plasmon wave packet arrives at position C at time $t = 41.3 \text{ fs}$ after the arrival of the pump pulse traveling from position B. Since the pump at position B is synchronized with the generation of the PSP wave, we only need to establish the probe travel time from position B to C and add 41.3 fs to get the time required for the PSP to travel 135 μm . The probe beam takes time $t = ((d \sin(75^\circ))/c) = 433.4 \text{ fs}$ to travel from B to C. Therefore, $t_{\text{plasmon}} = 433.4 + 41.3 = 474.7 \text{ fs}$, the time required for the plasmon to travel 135 μm . This results in a

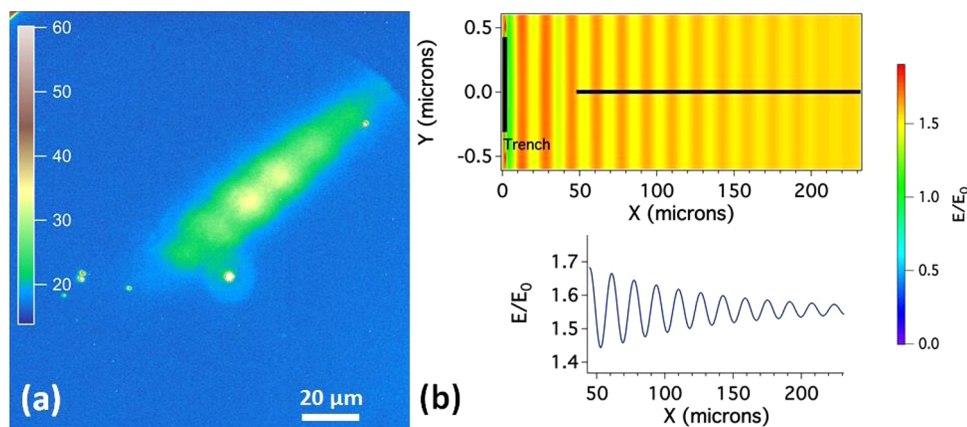


Figure 4. (a) PEEM image of the photoemission interference pattern $250 \mu\text{m}$ away from the plasmonic coupling structure. (b) The upper image displays FDTD results for E/E_0 from a $1 \mu\text{m} \times 1 \mu\text{m}$ trench etched into gold and illuminated with an 800 nm plane wave at 75° angle of incidence. The lower trace displays E/E_0 for the line profile drawn in the upper image.

group velocity of $0.95c \pm 0.01c$ for the propagating surface plasmon wave packet. The accuracy of the group velocity is limited only by our ability to measure a calibrated distance in the PEEM, and an accurate measurement of the laser angle of incidence ($\pm 1^\circ$). Because the pump–probe pulses are interferometrically locked, the pump–probe delay and hence the PSP arrival time is known to an accuracy better than 0.2 fs .

As previously mentioned, the PSP arriving at point C is temporally and spatially broadened. That said, the ability to transmit coherent signals via a PSP over large distances is determined by the spatial profile of the wave packet. This intensity is related to the initial light-surface plasmon coupling efficiency, attenuation constant, and dephasing rate. It is not trivial to comment on the initial coupling efficiency accurately at present, due to the complex spatial profiles of the pulses, and the nonlinearity of the response. However, it is clear from Figure 3b that the PSP wave packet is readily detected at distances greater than $100 \mu\text{m}$ from the trench coupling structure.

Figure 4a displays a TR-PEEM image of the plasmon-probe field interference pattern at a position $250 \mu\text{m}$ from the plasmonic coupling structure. The PEEM instrument has a maximum field-of-view (FOV) of $150 \mu\text{m}$. Nonetheless, we can still detect the PSP by moving the pump beam and coupling structure outside of the FOV and by detecting the PSP wave packet over $\sim 250 \mu\text{m}$ from the coupling trench, which indicates a relatively long propagation length. Still, the elliptical Gaussian shaped laser beam profiles and necessary spatial separation of pulses together render quantitative measurements of PSP propagation length challenging. Therefore, we rely on FDTD simulations of an analogous system to estimate these properties, and bridge the gap imposed by instrumental limitations. Figure 4b displays FDTD results from a single $1.0 \mu\text{m} \times 1.0 \mu\text{m}$ trench etched into gold and illuminated with a plane wave. The upper image displays the field (E/E_0) due to the interference of the one-photon generated plasmon field and the plane wave excitation field. A line profile through this image reveals the decay of this field, predominantly arising from the decay of the plasmon field as the plane wave excitation spans the simulation region both spatially and temporally. The $0\text{--}50 \mu\text{m}$ region is excluded from the profile because of interference from PSPs generated at the upper and lower corners of the trench. We recently showed that a similar effect governs the

photoemission images recorded following ultrafast irradiation of micron-sized holes etched in gold²⁸

The PSP decay length can be determined from the FDTD simulation by fitting the E/E_0 field to an exponentially damped sinusoidal function. The results indicate a $1/e$ decay parameter of $88 \mu\text{m}$. We note that this simulation necessarily utilizes relatively long pulses (160 fs, see Methods Section) and therefore does not include significant dispersion effects inherent in the experiment. The inherent dispersion, due to short pulse excitation, reduces the propagation length. Therefore, our calculated PSP decay length of $88 \mu\text{m}$ should be considered as an upper limit. That said, the calculated value, presented here, is consistent with, although larger than, a value of $60.3 \mu\text{m}$ estimated using eq 1 of ref 38 and the optical dielectric function tabulated in that article. A previous report also noted a discrepancy between the conventionally calculated and experimentally measured values, with the experimentally measured propagation length value being somewhat greater than the calculated one.⁴¹ The FDTD results can also be used to determine the group velocity by measuring the plasmon propagation time as a function of distance from the generating trench. A group velocity of $0.96c$ can be computed from our FDTD simulations, consistent with our above-described experimentally measured value.

Our results indicate that it is possible to launch a coherent PSP wave packet using a simple trench structure using a first-order process. The generated surface plasmon propagates for distances in excess of $250 \mu\text{m}$ and times longer than 500 fs . The use of spatiotemporally offset pump and probe pulse pairs allows the determination of the plasmon group velocity, measured to be $0.95c$. A combination of tr-PEEM and FDTD simulations reveals that the upper limit for the $1/e$ decay length of the plasmon field is $88 \mu\text{m}$. The experimentally measured PSP properties demonstrate that surface plasmons propagating on nominally flat gold surfaces may potentially be harnessed for use in mesoscale plasmonic devices, chiefly incorporated into plasmonic circuits of a few hundred microns in size.

Methods. A rectangular $10 \times 8 \mu\text{m}^2$ trench coupling structure was milled into a 100 nm thick gold thin film using focused ion beam lithography and imaged using a scanning electron microscope (FEI QUANTA SEM/GaFIB). The roughness of the otherwise flat sputtered gold film is $\sim 3 \text{ nm}$ (rms), consistent with previously reported values for thin Au films prepared using physical vapor deposition.⁴² The photo-

emission electron microscope (PEEM III, Elmitec, GmbH) is described elsewhere.²⁰ Briefly, femtosecond laser pulses (90 MHz repetition rate) were generated using a commercial titanium–sapphire femtosecond oscillator (Griffin-10, KM Laboratories), which produces 15 fs pulses (temporal full width) as measured using a frequency resolved optical gating (FROG) technique. The p-polarized laser beam is either used directly, or split into a “pump” and “probe” pair for time-resolved measurements. The incident laser sources are focused onto the sample surface using a 20 cm focal length lens, at an incident angle of 75° with respect to the surface normal. Under these conditions, elliptically shaped focused laser spots are observed, featuring major/minor axes of 120/20 μm.

Interferometrically locked fs pulse pairs were generated using a Mach-Zender interferometer.⁴³ A 50% beamsplitter produces pulses with comparable intensities in both arms of the interferometer. One arm contains a piezo-motor driven translation stage for coarse time delay between the pulses, while the other arm contains a mirror mounted on a piezoelectric transducer for fine control of the relative phase difference. The two pulses are recombined on a second 50% beamsplitter with one arm proceeding to the experimental apparatus and the other focused into a 1/8 m monochromator to generate the error signal used to interferometrically lock the two pulses.⁴³ A small displacement from a collinear geometry ensures that the pulses retain adequate overlap for interferometric control, while still providing small (\sim 150 μm) separation at the focal point at the sample surface. For a given time delay, PEEM images are averaged for 1 s and the delay step is 0.2 fs, creating a time-resolved movie, with each frame separated by the time step. Specific regions of interest within the movie can be extracted to obtain interferometric time-resolved data at select regions in space.

Numerical simulations were performed using a commercial FDTD package (Lumerical FDTD Solutions). The calculations model a 100 nm deep 1 μm × 1 μm trench etched in an infinitely thick gold film and span a total distance of 240 μm in the propagation direction. A plane wave source is used, injected at a 75 degree angle of incidence. The trench size and simulation dimensions are chosen to provide an accurate reproduction of the experiment, without resulting in prohibitively long simulation times. Model laser pulses of 160 fs are used both to ensure that the angular dispersion in injected wave vector is minimized, and to ascertain that the interference of the pump and plasmon fields occurs over the full region of the simulation. The dielectric permittivity of gold is taken from values for an evaporated gold film in a recent report.³⁸

■ ASSOCIATED CONTENT

Supporting Information

A log–log plot of the photoemission yield versus laser power indicating a three-photon power dependence measured at position 1 of Figure 2. A PEEM image of the photoemission interference pattern as described in the main text and a cross section and spatial widths of photoemission recurrences as a function of propagation distance. A movie displaying a propagating surface plasmon by time sequence of PEEM images, obtained using progressive pump–probe delays, is also provided. This material is available free of charge via the Internet at <http://pubs.acs.org>.

■ AUTHOR INFORMATION

Corresponding Author

*E-mail: wayne.hess@pnnl.gov.

Notes

The authors declare no competing financial interest.

■ ACKNOWLEDGMENTS

All authors acknowledge support from the US Department of Energy (DOE), Office of Science, Office of Basic Energy Sciences, Division of Chemical Sciences, Geosciences & Biosciences. P.Z.E. acknowledges support from the Laboratory Directed Research and Development Program through a Linus Pauling Fellowship at Pacific Northwest National Laboratory (PNNL). A portion of the work was performed using EMSL, a national scientific user facility sponsored by the DOE's Office of Biological and Environmental Research and located at PNNL. PNNL is a multiprogram national laboratory operated for DOE by Battelle.

■ REFERENCES

- (1) Bai, M.; Guerrero, C.; Ioanid, S.; Paz, E.; Sanz, M.; Garcia, N. *Phys. Rev. B* **2004**, *69*, 115416.
- (2) Gramotnev, D. K.; Bozhevolnyi, S. I. *Nat. Photonics* **2010**, *4*, 83–91.
- (3) MacDonald, K. F.; Sámsón, Z. L.; Stockman, M. I.; Zheludev, N. I. *Nat. Photonics* **2009**, *3*, 55–58.
- (4) Cao, L.; Brongersma, M. L. *Nat. Photonics* **2009**, *3*, 12–13.
- (5) Kriesch, A.; Burgos, S. P.; Ploss, D.; Pfeifer, H.; Atwater, H. A.; Peschel, U. *Nano Lett.* **2013**, *13*, 4539–4545.
- (6) Briggs, R. M.; Grandidier, J.; Burgos, S. P.; Feigenbaum, E.; Atwater, H. A. *Nano Lett.* **2010**, *10*, 4851–4857.
- (7) Pettinger, B.; Schambach, P.; Villagómez, C. J.; Scott, N. *Annu. Rev. Phys. Chem.* **2012**, *63*, 379–399.
- (8) Stadler, J.; Schmid, T.; Zenobi, R. *Nanoscale* **2012**, *4*, 1856–1870.
- (9) Le Ru, E. C.; Etchegoin, P. G. *Annu. Rev. Phys. Chem.* **2012**, *63*, 65–87.
- (10) Banik, M.; El-Khoury, P. Z.; Nag, A.; Rodriguez-Perez, A.; Guarrotxena, N.; Bazan, G. C.; Apkarian, V. A. *ACS Nano* **2012**, *6*, 10343–10354.
- (11) Chang, W. S.; Lassiter, J. B.; Swanglap, P.; Sobhani, H.; Khatua, S.; Nordlander, P.; Halas, N. J.; Link, S. *Nano Lett.* **2012**, *12*, 4977–4982.
- (12) Wild, B.; Cao, L. N.; Sun, Y. G.; Khanal, B. P.; Zubarev, E. R.; Gray, S. K.; Scherer, N. F.; Pelton, M. *ACS Nano* **2012**, *6*, 472–482.
- (13) Solis, D.; Paul, A.; Chang, W. S.; Link, S. *J. Phys. Chem. B* **2013**, *117*, 4611–4617.
- (14) Nauert, S.; Paul, A.; Zhen, Y. R.; Solis, D.; Vigderman, L.; Chang, W. S.; Zubarev, E. R.; Nordlander, P.; Link, S. *ACS Nano* **2014**, *8*, 527–580.
- (15) Liu, X. J.; Wang, Y.; Potma, E. O. *Appl. Phys. Lett.* **2012**, *101*, 081116.
- (16) Cheng, J. X.; Xie, X. S. *Coherent Raman Scattering Microscopy*; CRC Press: Boca Raton, 2013.
- (17) Egorov, D.; Dennis, B. S.; Blumberg, G.; Haftel, M. I. *Phys. Rev. B* **2004**, *70*, 033404.
- (18) Kubo, A.; Pontius, N.; Petek, H. *Nano Lett.* **2007**, *7*, 470–475.
- (19) Zhang, L. X.; Kubo, A.; Wang, L. M.; Petek, H.; Seideman, T. *Phys. Rev. B* **2011**, *84*, 245442.
- (20) Peppernick, S. J.; Joly, A. G.; Beck, K. M.; Hess, W. P. *J. Chem. Phys.* **2011**, *134*, 034507.
- (21) Cinchetti, M.; Gloskovskii, A.; Nepjiko, S. A.; Schönhense, G.; Rochholz, H.; Kreiter, M. *Phys. Rev. Lett.* **2005**, *95*, 047601.
- (22) Meyer zu Heringdorf, F.-J.; Chelaru, L. I.; Möllenbeck, S.; Thien, D.; Horn-von Hoegen, M. *Surf. Sci.* **2007**, *601*, 4700–4705.
- (23) Kubo, A.; Onda, K.; Petek, H.; Sun, Z. J.; Jung, Y. S.; Kim, H. K. *Nano Lett.* **2005**, *5*, 1123–1127.

- (24) Yin, L.; Vlasko-Vlasov, V. K.; Rydh, A.; Pearson, J.; Welp, U.; Chang, S. H.; Gray, S. K.; Schatz, G. C.; Brown, D. B.; Kimball, C. W. *Appl. Phys. Lett.* **2004**, *85*, 467–469.
- (25) Lee, K. G.; Park, Q. H. *Phys. Rev. Lett.* **2005**, *95*, 103902.
- (26) Polyakov, A.; Senft, C.; Thompson, K. F.; Feng, J.; Cabrini, S.; Schuck, P. J.; Padmore, H. A.; Peppernick, S. J.; Hess, W. P. *Phys. Rev. Lett.* **2013**, *110*, 076802.
- (27) Day, J. K.; Neumann, O.; Grady, N. K.; Halas, N. J. *ACS Nano* **2010**, *4*, 7566–7572.
- (28) Gong, Y.; Joly, A. G.; El-Khoury, P. Z.; Hess, W. P. *J. Phys. Chem. C* **2014**, *118*, 25671–25676.
- (29) Gong, Y.; Joly, A. G.; El-Khoury, P. Z.; Hess, W. P. *J. Phys. Chem. Lett.* **2014**, *5*, 4243–4248.
- (30) Sobhani, A.; Knight, M. W.; Wang, Y. M.; Zheng, B.; King, N. S.; Brown, L. V.; Fang, Z. Y.; Nordlander, P.; Halas, N. J. *Nat. Commun.* **2013**, *4* (1643), 1–6.
- (31) Wang, Y.; Liu, X. J.; Whitmore, D.; Xing, W. D.; Potma, E. O. *Opt. Express* **2011**, *19*, 13454–13463.
- (32) Barnes, W. L.; Dereux, A.; Ebbesen, T. W. *Nature* **2003**, *424*, 824–830.
- (33) Kubo, A.; Jung, Y. S.; Kim, H. K.; Petek, H. *J. Phys. B-At. Mol. Opt.* **2007**, *40*, S259–S272.
- (34) Zhang, L. X.; Kubo, A.; Wang, L. M.; Petek, H.; Seideman, T. J. *Phys. Chem. C* **2013**, *117*, 18648–18652.
- (35) Lemke, C.; Schneider, C.; Leißner, T.; Bayer, D.; Radke, J. W.; Fischer, A.; Melchior, P.; Evlyukhin, A. B.; Chichkov, B. N.; Reinhardt, C.; Bauer, M.; Aeschlimann, M. *Nano Lett.* **2013**, *13*, 1053–1058.
- (36) Lemke, C.; Leißner, T.; Evlyukhin, A.; Radke, J. W.; Klick, A.; Fiutowski, J.; Kjelstrup-Hansen, J.; Rubahn, H. G.; Chichkov, B. N.; Reinhardt, C.; Bauer, M. *Nano Lett.* **2014**, *14*, 2431–2435.
- (37) Wang, L. M.; Petek, H. *Laser Photonics Rev.* **2013**, *7*, 1003–1009.
- (38) Olmon, R. L.; Slovick, B.; Johnson, T. W.; Shelton, D.; Oh, S. H.; Boreman, G. D.; Raschke, M. B. *Phys. Rev. B* **2012**, *86*, 235147.
- (39) Nagel, P. M.; Robinson, J. S.; Harteneck, B. D.; Pfeifer, T.; Abel, M. J.; Prell, J. S.; Neumark, D. M.; Kaindl, R. A.; Leone, S. R. *Chem. Phys.* **2013**, *414*, 106–111.
- (40) Schmidt, O.; Bauer, M.; Wiemann, C.; Porath, R.; Scharte, M.; Andreyev, O.; Schönhense, G.; Aeschlimann, M. *Appl. Phys. B: Laser Opt.* **2002**, *74*, 223–227.
- (41) Koev, S. T.; Agrawal, A.; Lezec, H. J.; Aksyuk, V. A. *Plasmonics* **2012**, *7*, 269–277.
- (42) Melli, M.; Polyakov, A.; Gargas, D.; Huynh, C.; Scipioni, L.; Bao, W.; Ogletree, D. F.; Schuck, P. J.; Cabrini, S.; Weber-Bargioni, A. *Nano Lett.* **2013**, *13*, 2687–2691.
- (43) Scherer, N. F.; Carlson, R. J.; Matro, A.; Du, M.; Ruggiero, A. J.; Romero-rochin, V.; Cina, J. A.; Fleming, G. R.; Rice, S. A. *J. Chem. Phys.* **1991**, *95*, 1487–1511.